VARIABLE MAGNETIC STIFFNESS APPROACH FOR SIMULTANEOUS SENSOR RUNOUT AND MASS UNBALANCE COMPENSATION IN ACTIVE MAGNETIC BEARINGS

Joga D. Setiawan and Ranjan Mukherjee
Michigan State University, East Lansing, Michigan, USA, mukherji@egr.msu.edu
Eric H. Maslen
University of Virginia, Charlottesville, Virginia, USA, ehm7s@virginia.edu

ABSTRACT
This paper proposes a new approach for simultaneous compensation of two synchronous periodic disturbances in active magnetic bearings (AMB's); sensor runout (SRO) and mass unbalance. Using Lyapunov's method, a novel adaptive algorithm is developed to uniquely determine the harmonic components of both disturbances and guarantee asymptotic stability of the rotor geometric center about the origin. By varying magnetic stiffness through excitation of the bias currents, the system achieves a persistently exciting condition that ensures exponential convergence of estimated parameters to the true values. The algorithm is superior to existing techniques since the identification process can be performed without changing rotor angular speed. Both simulation and experimental results validate the effectiveness of the algorithm.

INTRODUCTION
The dominant sources of synchronous periodic disturbances in magnetic bearings are unbalance, which generates disturbance at the first harmonic of rotation, and sensor runout, which generates disturbance at multiple harmonics. While unbalance results from lack of alignment between the geometric axis and the principal axis of inertia, sensor run-out results from lack of concentricity of the sensing surface and non-uniform electrical or magnetic properties around it. Our research will specifically address the problem of synchronous mass unbalance and sensor run-out compensation and provide the scope for rotor stabilization about the geometric center.

There have been numerous studies on periodic disturbance compensation [1-3]. Unfortunately, most of the approaches found in the literature do not lend themselves to runout estimation in the presence of significant mass unbalance. This problem, widely acknowledged in the literature but essentially unsolved, stems from a lack of observability of disturbances with the same frequency content. A credible way to distinguish between these disturbances is to perturb the operating conditions of the plant or its parameters. However, recent studies [4-5] that propose variation in rotor angular speed as a means to enhance observability may not be acceptable for most applications. Our approach to the problem is based on traditional adaptive control designs that has seen applications with a variety of electromechanical systems [6] but not magnetic bearings. In our approach, we will individually identify synchronous mass unbalance and sensor run-out at constant rotor speed through persistency of excitation.

MAGNETIC BEARING MODEL
Consider the rigid rotor in Fig. 1. Under magnetic levitation, the rotor has two degrees of freedom along the x and y axes; the displacements along these axes are measured by non-contact gap sensors. The dynamics of the rotor along these axes, which are both inclined at 45° with the horizontal, are decoupled but similar. Along the x axis, one may write

$$m\,\ddot{x} = F - m\,\bar{g} + f_u, \qquad \bar{g} \triangleq g/\sqrt{2} \tag{1}$$

where m is the mass of the rotor, x is the rotor position, F is the magnetic force, f_u is the unbalance force, and g is the gravity. The magnetic force can be expressed as

$$F = k\left[\left(\frac{i_{10}+I}{l-x}\right)^2 - \left(\frac{i_{20}-I}{l+x}\right)^2\right] \tag{2}$$

where k is the magnetic force constant, l is the nominal air gap, i_{10}, i_{20} are the bias currents in the top and bottom electromagnets, and I is the control current. By linearizing Eq.(2) about $x = 0$, $I = 0$, Eq.(1) can be written as

$$m\,\ddot{x} = K_s x + f_c + f_u, \quad f_c \triangleq K_c I \tag{3}$$

$$K_s \triangleq 2k\left(i_{10}^2 + i_{20}^2\right)/l^3, \quad K_c \triangleq 2k\left(i_{10} + i_{20}\right)/l^2 \tag{4}$$

where f_c is the control force, K_s and K_c are the magnetic stiffness and actuator gain of the magnetic bearing respectively. The mass unbalance force can be modeled as

$$f_u = m\,\omega^2\,[\,p\sin(\omega t) + q\cos(\omega t)] \tag{5}$$

where $p = -\varepsilon\sin(\theta_u)$, $q = \varepsilon\cos(\theta_u)$, θ_u is the phase of unbalance, ω is the rotor angular speed, and ε is the eccentricity of the rotor.

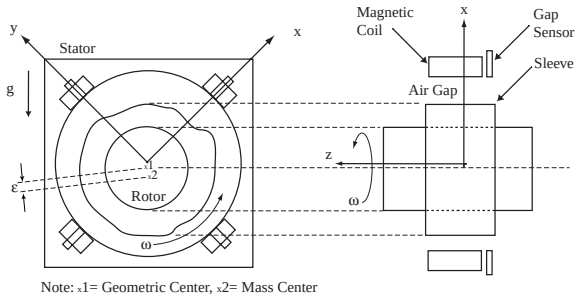

FIGURE 1: Magnetic bearing-rotor schematic

The true location of the rotor geometric center is not available for a magnetic bearing with sensor runout. Instead, the gap sensors provide the signal x_s.

$$x_s = x + d \tag{6}$$

where, d, the SRO disturbance that can be expressed by the Fourier series

$$d \triangleq a_0 + \sum_{i=1}^{n} a_i\,\sin(i\omega t) + b_i\,\cos(i\omega t) \tag{7}$$

In the above expression, n is the number of harmonics, a_0 is the DC component, and a_i, b_i, $i = 1, 2, \ldots, n$, are the harmonic Fourier coefficients.

ADAPTIVE CONTROL DESIGN

Preliminary

In this section we introduce an adaptive control framework for stabilization of the rotor geometric center to the origin. As shown in Fig. 2, the controller is an on-line feedforward type. It consists of two main components: the feedback law to stabilize the closed loop system and the adaptation law to estimate the two periodic disturbances f_u and d simultaneously. We define the estimated geometric position

$$\bar{x} \triangleq x_s - \hat{d} \tag{8}$$

$$\hat{d} \triangleq \hat{a}_0 + \sum_{i=1}^{n} \hat{a}_i\,\sin(i\omega t) + \hat{b}_i\,\cos(i\omega t) \tag{9}$$

In the above expression, $\hat{a}_0$ is the estimated value of a_0, and $\hat{a}_i$, $\hat{b}_i$ are estimated values of a_i, b_i, respectively, for $i = 1, 2, \ldots, n$. Using Eqs.(6), (8) and (9), we obtain

$$\bar{x} = x + \tilde{d}, \quad \tilde{d} \triangleq (d - \hat{d}) = \mathbf{Y}^T\tilde{\phi} \tag{10}$$

where, $\tilde{d}$, the error in the estimate of sensor runout disturbance. The regressor vector $\mathbf{Y}$, and the vector of parameter estimation errors $\tilde{\phi}$, are defined as

$$\mathbf{Y} \triangleq [\,1 \quad \sin(\omega t) \quad \cos(\omega t) \quad \ldots \quad \sin(n\omega t) \quad \cos(n\omega t)\,]^T$$

$$\tilde{\phi}^T \triangleq \begin{bmatrix} \tilde{a}_0 & \tilde{\phi}_\alpha^T & \tilde{\phi}_\beta^T \end{bmatrix}$$

where
$\tilde{\phi}_\alpha \triangleq \begin{bmatrix} \tilde{a}_1 & \tilde{b}_1 \end{bmatrix}^T$, $\tilde{\phi}_\beta \triangleq \begin{bmatrix} \tilde{a}_2 & \tilde{b}_2 & \ldots & \tilde{a}_n & \tilde{b}_n \end{bmatrix}^T$, $\tilde{a}_0 \triangleq (a_0 - \hat{a}_0)$, and $\tilde{a}_i \triangleq (a_i - \hat{a}_i)$, $\tilde{b}_i \triangleq (b_i - \hat{b}_i)$, $i = 1, 2, \ldots, n$.
The estimate of the unbalance force is defined as

$$\hat{f}_u \triangleq -\mathbf{Y}_u^T\hat{\phi}_u \tag{11}$$

where $\mathbf{Y}_u^T \triangleq -m\omega^2\,[\sin(\omega t) \quad \cos(\omega t)]$ and $\hat{\phi}_u \triangleq [\hat{p} \quad \hat{q}]^T$. The terms $\hat{p}$ and $\hat{q}$ are estimates of Fourier coefficients p and q respectively. Thus, we can write the errors in the estimation as $\tilde{p} = p - \hat{p}$ and $\tilde{q} = q - \hat{q}$, or in vector form

$$\tilde{\phi}_u \triangleq [\,\tilde{p} \quad \tilde{q}\,] \tag{12}$$

For the variable magnetic stiffness approach, we intend to excite the top and bottom bias currents i_{10} and i_{20} by δ_1 and δ_2 in the following manner:

$$i_{10} = i_{10}^* + \delta_1, \qquad i_{20} = i_{20}^* + \delta_2 \tag{13}$$

where i_{10}^* and i_{20}^* are constant bias current in the top and bottom coils. We denote

$$K_s^* \triangleq 2k\,(i_{10}^{*2} + i_{20}^{*2})\,/l^3, \quad K_c^* \triangleq 2k\,(i_{10}^* + i_{20}^*)\,/l^2$$

By choosing $\delta_2 = \frac{i_{10}^*}{i_{20}^*}\delta_1$, we can verify using linearizaton of Eq.(2) that this excitation produces zero bias force about the origin. We can rewrite Eq.(4) as

$$K_s = K_s^* + \frac{8ki_{10}^*}{l^3}\delta_1, \quad K_c = K_c^* + \frac{2k}{l^2}\left(1 + \frac{i_{10}^*}{i_{20}^*}\right)\delta_1 \tag{14}$$

For simplicity, we use $\delta_1 = A\sin(2\pi ft)$ where A is the amplitude of excitation and f is the excitation frequency. This frequency will be chosen to be smaller enough compared to the rotor rotation frequency. By choosing a relatively small A, we may assume that the effect of the excitation to the net magnetic force in Eq.(2) is negligible.

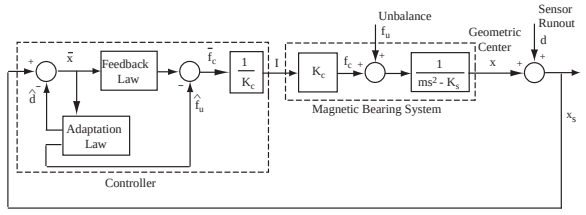

FIGURE 2: Adaptive SRO and Unbalance Compensation Framework

Theoretical Development

With the objective of stabilizing x to the origin, we propose a Lyapunov function candidate

$$V = \frac{1}{2}\left[(1-\Delta)m\bar{e}^2 + \widetilde{\phi}^T\Gamma^{-1}\widetilde{\phi} + \widetilde{\phi}_u^T\Gamma_u^{-1}\widetilde{\phi}_u\right] \quad (15)$$

where $\Gamma \triangleq diag(\gamma_0, \gamma_1, \gamma_1, \ldots, \gamma_n, \gamma_n)$, $\Gamma_u \triangleq diag(\gamma_p, \gamma_q)$ for $\gamma_p, \gamma_q > 0$, and

$$\bar{e} \triangleq \dot{\bar{x}} + \lambda\bar{x}, \qquad \lambda > 0 \quad (16)$$

The constants $\gamma_0, \gamma_1, \ldots, \gamma_n$ are positive and chosen such that $0 < \Delta < 1$, where

$$\Delta \triangleq \mathbf{Y}^T\Gamma\mathbf{Y}_m = \sum_{i=0}^{n}\gamma_i\left(K_s + m(i\omega)^2\right) \quad (17)$$

$$\mathbf{Y}_m \triangleq K_s\mathbf{Y} - m\ddot{\mathbf{Y}} \quad (18)$$

Since K_s is time varying and $\dot{\mathbf{Y}}^T\Gamma\mathbf{Y}_m = 0$, we get

$$\dot{\Delta} = \mathbf{Y}^T\Gamma\dot{\mathbf{Y}}_m = \dot{K}_s\sum_{i=0}^{n}\gamma_i \quad (19)$$

Knowing that the excitation δ_1, causes the actuator gain K_c to vary, the control current $I = f_c/K_c$ in Eq.(3) should be computed with a time varying K_c using Eq.(14). By choosing the control force

$$f_c = -K_s\bar{x} - m\lambda\dot{\bar{x}} - (c + \frac{1}{2}m\dot{\Delta})\bar{e} - \hat{f}_u \quad (20)$$

along with adaptation laws

$$\dot{\widetilde{\phi}} = \mathbf{\Gamma}\,\mathbf{Y}_m\,\bar{e}, \quad \dot{\widetilde{\phi}}_u = \mathbf{\Gamma}_u\,\mathbf{Y}_u\,\bar{e} \quad (21)$$

we can conclude that the closed loop system is stable and all components of the estimate parameters $\hat{\phi}$ and $\hat{\phi}_u$ converge to their true values. The proof is as follows. Using Eq.(3) and Eqs.(15-21) the dynamics of the system can be described by

$$m(1-\Delta)\dot{\bar{e}} = -\mathbf{Y}_m^T\widetilde{\phi} + \frac{1}{2}m\dot{\Delta}\bar{e} - c\bar{e} - \mathbf{Y}_u^T\widetilde{\phi}_u \quad (22)$$

The derivative of the Lyapunov function in Eq.(17) can be easily shown to be $\dot{V} = -c\bar{e}^2 \leq 0$. Knowing $\ddot{V}$ is uniformly continuous, from Barbalat's Lemma [7], we can claim that $\dot{V} \to 0 \Rightarrow \bar{e} \to 0$. Taking derivative of Eq.(22), we can show that $\ddot{\bar{e}}$ is bounded $\Rightarrow \dot{\bar{e}}$ is uniformly continous $\Rightarrow \dot{\bar{e}} \to 0$. Therefore, from Eq.(22) we can argue that

$$\begin{bmatrix}\mathbf{Y}_m^T & \mathbf{Y}_u^T\end{bmatrix}\begin{bmatrix}\widetilde{\phi} \\ \widetilde{\phi}_u\end{bmatrix} \to 0 \quad \text{as} \quad t \to \infty \quad (23)$$

By defining $\mathbf{Y}_{mu}^T \triangleq \begin{bmatrix}\mathbf{Y}_m^T & \mathbf{Y}_u^T\end{bmatrix}$, we can verify that $\mathbf{Y}_{mu}^T$ is a persistently exciting (PE) regressor vector [7] since

$$\alpha_2\mathbf{I} > \int_{t}^{t+T_o}\mathbf{Y}_{mu}\mathbf{Y}_{mu}^T d_T > \alpha_1\mathbf{I}$$

where α_1, α_2, and T_o are positive constants and $\mathbf{I}$ is a 2n+3 by 2n+3 identity matrix, we can conclude that $\widetilde{\phi} \to 0$ and $\widetilde{\phi}_u \to 0$. Thus, the PE condition of $\mathbf{Y}_{mu}^T$, guarantees $\hat{a}_0$, $\hat{a}_i$ and $\hat{b}_i$ for $i = 1, \ldots, n$ and $\hat{p}$ and $\hat{q}$ all to converge to their true values and x to converge to the origin. It should be noted that this PE condition is satisfied only because of the bias current excitation described in Eqs. (13-14).

TABLE 1: Parameters for Simulation

Gains:	$\lambda = 400\,s^{-1}, \quad c = 1200\,kg/s$ $\Gamma = diag(1.4, 3, 3, 3, 3) \times 10^{-7}\,m/N$ $\Gamma_u = diag(3, 3) \times 10^{-5}\,m/N$
IC's:	$x(t=0) = -100\,\mu m/s$ $\dot{x}(t=0) = 0$ $\hat{\phi}(t=0) = \mathbf{0}, \quad \hat{\phi}_u(t=0) = \mathbf{0}$
SRO:	$a_0 = 2.5\,\mu m$ $a_1 = 18.35\,\mu m, \quad b_1 = 4.92\,\mu m$ $a_2 = 1.77\,\mu m, \quad b_2 = 1.77\,\mu m$
Unbalance:	$p = 86.6\,\mu m, \quad q = 50.0\,\mu m$

SIMULATION RESULTS

Simulation results are presented in Figs. 3, 4 and 5 to demonstrate the effectiveness of the Variable Magnetic Stiffness approach. For simulation, we used the nonlinear plant model in Eqs.(1) and (2), parameters in Tables 1 and 2 and the rotor angular speed of $1500\,rpm$. The SRO identification was performed for up to the second harmonic only. In the simulation, we turned on the bias current excitation at time interval $5 < t < 35\,s$ using an amplitude of $0.2\,A$ and frequency of $10\,Hz$.

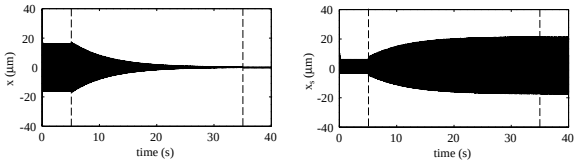

FIGURE 3: Geometric center x and sensor signal with runout x_s

As seen in Fig. 3, for $t < 5\,s$, the geometric center oscillates with constant amplitude due to sensor runout and unbalance. Without bias current excitation, Fig. 4 indicates that for $t < 5\,s$ the estimated parameters $\hat{a}_1$, $\hat{b}_1$, $\hat{p}$, and $\hat{q}$ converge to arbitrary values while $\hat{a}_0$, $\hat{a}_2$ and $\hat{b}_2$ converge to to the true values. After we turned on the bias current excitation, the parameters $\hat{a}_1$, $\hat{b}_1$, $\hat{p}$, and $\hat{q}$ converge to the true values within $30\,s$ which results to the stabilization of the geometric center about the origin shown in Fig. 3. During the excitation, in Fig. 4 we can observe a diminishing slight fluctuation of the parameters $\hat{a}_0$, $\hat{a}_2$

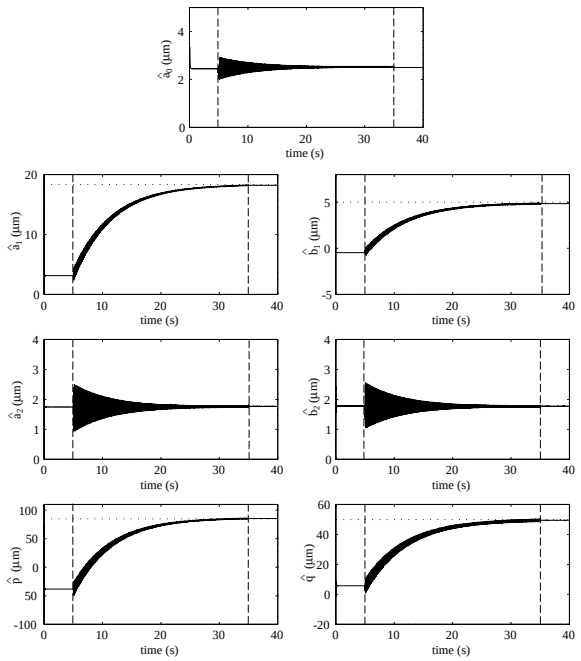

FIGURE 4: Estimated Fourier coefficients; dotted lines are the true values

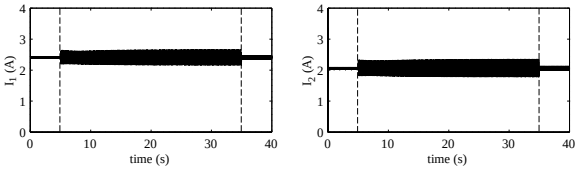

FIGURE 5: Top and bottom bias currents

and $\hat{b}_2$ about the true values. As shown in Figs. 3 and 4, after all parameters have converge to the true values i.e. $t > 35$, turning off the excitation has negligible effect. The geometric center remains at the origin and the estimated parameters stay at the true values. Turning off the exitation at this time has an advantage of reducing efforts in the power amplifier as seen in Fig. 5.

EXPERIMENTAL VALIDATION

Experimental Setup and Procedure

The magnetic bearing test rig shown in Fig. 6 was set up to validate the effectiveness of the Variable Magnetic Stiffness approach. The parameters of the half-rotor assembly and bearing and the operating conditions are shown in Table 2.

The rotor shaft is $60.2\,cm$ long and $2.5\,cm$ in diameter. At the midspand of the shaft, we placed a balanced disk that allowed trial weights to be attached. We anticipated that in this arrangement, the shaft's first flexible mode occured at $450\,Hz$, which was six times higher than the closed-loop magnetic bearing control bandwidth. We used an 8-bit absolute-analog encoder to track the angular position of the rotor and provide the value of $\Theta = \omega\, t$. The

TABLE 2: Magnetic Bearing Test Rig Parameters

Parameter	Value
Rotor mass, m	$2.43\,kg$
Electromagnetic force constant, k	$2.82 \times 10^{-6}\,Nm^2/A^2$
Nominal air gap, l	$0.508 \times 10^{-3}\,m$
Top bias current, i^*_{10}	$2.41\,A$
Bottom bias current, i^*_{20}	$2.06\,A$
Actuator gain, K^*_c	$97.71\,N/A$
Magnetic stiffness, K^*_s	$4.33 \times 10^5\,N/m$

encoder was attached to one end of the rotor shaft using a torsionally rigid coupling as shown in Fig. 6. The coupling, however, is axially flexible and allows lateral misalignments such that it does not introduce additional radial force to the rotor shaft. A closed-loop circuit consist of an optical speed sensor, a proportional controller and an AC motor was used to maintain a constant rotor angular speed.

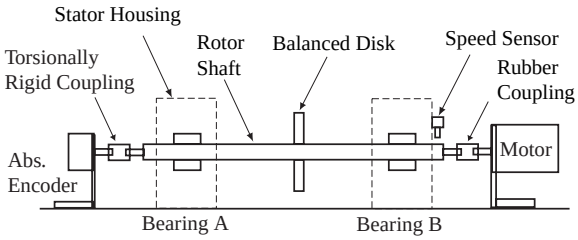

FIGURE 6: Magnetic bearing test rig schematic

The adaptive control algorithm was implemented in Matlab/Simulink^{TM} environment and downloaded to a DSP board, manufactured by dSPACE. The DSP board, sampling approximately at $13kHz$, was used to control the rotor along x axis in bearing A. Thus, the adaptive control verification was performed on one axis only. The remain three axes including the two axes in bearing B were controlled by analog PD controllers. The electromagnets were driven by switching amplifiers, a product of Advanced Motion Control, operating with $1.6\,kHz$ bandwidth.

In our experiment, we did not need to provide an additional SRO to the system since the runout was already considerably substantial. We utilized a separate DSP that sampled at $5\,kHz$ and analog circuits to generate the geometric center signal based on the pre-determined SRO. Thus, the trajectory of the geometric center was recovered and used to evaluate the performance of the adaptive algorithm. Our manual identification of the SRO revealed that the first harmonic component of the SRO was highly dominant in all axes. However, we assumed that the SRO effect from other axes to the axis being evaluated to be small since they were compensated using the predetermined SRO. In the x axis, the first harmonic components of the SRO were found to be $a_1 = 13.5\,\mu m$ and

$b_1 = 0\,\mu m$.

We set the adaptive control to identify up to the first harmonics for the SRO in the x axis. We initially levitated the rotor by setting the adaptation gains Γ and Γ_u, the excitation δ_1, and the estimated parameters $\hat{\phi}$ and $\hat{\phi}_u$ all to zero. At this time, the x axis was equivalent to being controlled by a simple PD controller with $\lambda = 400\,s^{-1}$, $c = 1200\,kg/s$ and $\dot{\Delta} = 0$. In controller implementation, the derivative of the estimated position signal, $\dot{\hat{x}}$, was numerically computed using the transfer function $2500/(s + 2500)$. We then increased the rotor angular speed from 0 to 1500 rpm. After the speed stayed constant at 1500 rpm, we started the adaptation by switching the adaptation gains to $\Gamma = diag(1.4, 3.0, 3.0) \times 10^{-7}\,m/N$, and $\Gamma_u = diag(3, 3) \times 10^{-5}\,m/N$. During this adaptation, we excited the system with δ_1 having an amplitude of $0.2\,A$ and frequency of $10\,Hz$. After the estimated parameters reached steady state values, we simultaneously set the adaptation gain to zero and stopped the excitation on the bias currents. We ran this experiment two times and recorded the final value of the estimated parameters at the end of each experiment. We then stopped the rotor and repeated the above procedure after placing a trial weight of $10\,g$ on the balanced disk. We ran this experiment twice to verify the consistency of the results.

Experimental Results

The steady-state values of the estimated parameters from the four experiments are tabulated in Table 3. Using $\hat{a}_1$ and $\hat{b}_1$, we computed the magnitude and the phase angle of the first harmonic of SRO, and included the results in Table 3. Similarly, we show the magnitude and the phase angle of the unbalance, knowing $\hat{p}$ and $\hat{q}$.

TABLE 3: Steady-State Values of Estimated Parameters in Experiment

	No m_t		With m_t	
	Exp.1	Exp.2	Exp.3	Exp.4
SRO:				
$\hat{a}_0$	-2.1	-1.4	-2.0	-2.8
$\hat{a}_1$	16	16	15	13
$\hat{b}_1$	0.68	1.0	-0.67	-0.7
Magnitude	16.0	16.0	15.0	13.0
Phase (^{o})	2	2	358	358
Unbalance:				
$\hat{p}$	76	82	130	120
$\hat{q}$	-26	-23	-8.1	-9.5
Magnitude	80.3	85.2	130	120
Phase (^{o})	251	254	266	267

Note: all dimensions in μm , except otherwise mentioned

We present in Fig. 7, the snapshots of x and x_s from experiment 3 to show five regions: 1) without adaptation at $t < 0\,s$, 2) initial adaptation at $0 < t < 0.3\,s$, 3) during adaptation at $t_1 < t < t_1 + 0.3\,s$, 4) end of adaptation $t_2 - 0.3 < t < t_2\,s$, and 5) after adaptation $t > t_2$. In this particular experiment, t_1 and t_2 were taken at about $60\,s$ and $110\,s$ respectively. It can be seen that the geometric center x initially fluctuated with an amplitude of $15\,\mu m$ about the mean value of $5\,\mu m$. At $t = 0\,s$ we started the adaptation together with the excitation of bias currents. It can be observed that within t_2 seconds the fluctuation in the geometric center has been reduced by 95 percent. Turning off the adaptation and excitation at $t = t_2$ resulted to even smaller fluctuation in x.

Due to our hardware limitation, we acquired the time traces of estimated parameters in a separate experiment. The time traces of estimated parameters obtained from experiment 4 are shown in Fig. 8. It can be observed that the estimated parameters converge to steady-state values within 110 seconds. During the transient the SRO parameters oscillates with amplitude less than $3\,\mu m$. The variation in the DC component is negligible.

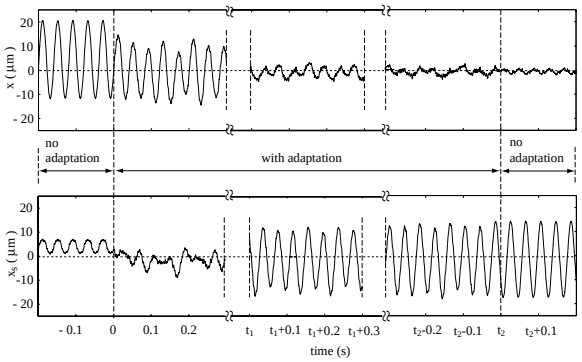

FIGURE 7: Snapshots of geometric center x and sensor signal with runout x_s (experiment 3 result)

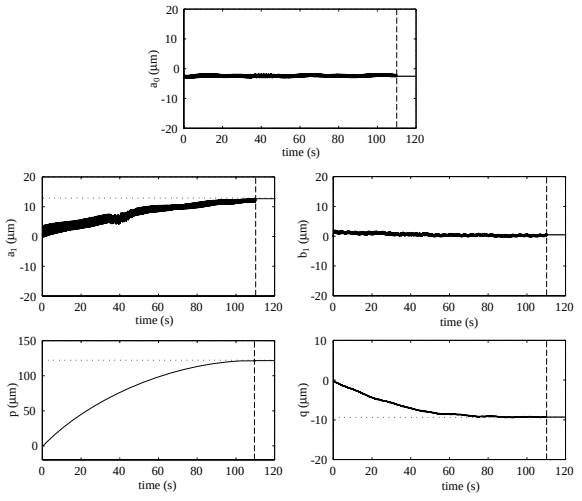

FIGURE 8: Time trace of estimated Fourier coefficients in experiment 4; dotted lines are final values shown in Table 3

The experimental results indicate that the first harmonic

components of the SRO in Table 3 have an average magnitude of $15\ \mu m$ and phase angle of 0^o. The variation in the magnitude and phase angle can be considered very small: within ± 10 percent in magnitude and $\pm 2^o$ in the phase angle. The experiments suggest that adding trial weight does not affect the first harmonic components of SRO. Thus, the experiments confirm the consistency of our plant model. It also can be seen that the results are very close to the pre-determined SRO: $a_1 = 13.5\ \mu m$ and $b_1 = 0$.

To verify the consistency of the results in the unbalance components, we may use a vector diagram. For example, using the vector diagram in Fig. 9 we can calculate the resultant unbalance force $\vec{A}_R$ and compare to the experimental results in Table 3. We may define the initial unbalance as $\vec{A}_u$ using the results of experiments 1 and 2 shown in Table 3. Using the average, we get $|\vec{A}_u| = 82.75\ \mu m$ and $\theta_u = 252.5^o$. Knowing the location and the mass of the trial weight we can find $\vec{A}_t$ and ready to calculate $\vec{A}_R = \vec{A}_u + \vec{A}_t$. From the physical and geometric data, our particular set-up yields $|\vec{A}_t| = 60\ \mu m$ and $\theta_t = 289^o$. Thus we can obtain $|\vec{A}_R| = 136\ \mu m$ and $\theta_R = 268^o$ which are very close to the experimental results in experiments 3 and 4 shown in Table 3.

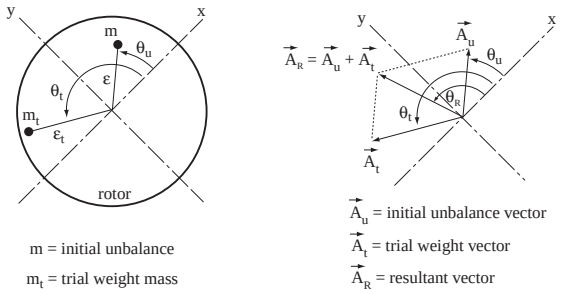

FIGURE 9: Verification using a trial weight

CONCLUSIONS

We have presented a new adaptive algorithm that can uniquely identify the harmonic components of sensor runout and unbalance. Both simulation and experimental results confirm that the approach can significantly improve the performance of a magnetically levitated rigid rotor by means of precise rotation about the geometric center.

The adaptive algorithm provides several advantages. First, the identification process can be performed without changing rotor angular speed. Secondly, in implementation the algorithm does not require extra hardware except an additional D/A channel to drive the top and bottom coils separately. Moreover, the algorithm allows us to turn the adaptation on and off when necessary without problem.

Future work should consider the effect of uncertainty on plant parameters.Robustness of the algorithm to rotor flexible modes should also be investigated. Extending the approach for a centralized magnetic bearing control system and the use of the approach in tandem with performance index minimization may also be valuable.

REFERENCES

1. Kim, C. -S., and Lee, C. -W., *In Situ Runout Identification in AMB System by Extended Influence Coefficient Method*, IEEE/ASME Trans. on Mechatronics, Vol.2, No.1, pp.51-57, 1997.
2. Knospe, C. R., Tamer, S. M., and Fedigan, S. J., *Robustness of Adaptive Rotor Vibration Control to Structured Uncertainty*, ASME J. of Dyn. Sys., Meas. and Cont., 119, pp.243-250, 1997.
3. Shafai, B., Beale, S., Larocca, P., and Cusson, E., *Magnetic Bearing Control Systems and Adaptive Forced Balancing*, IEEE Control Systems, 14, pp.4-13, 1994.
4. Kanemitsu, Y., Kijimoto, S., Matsuda, K., and Jin, P. T., *Identification and Control of Unbalance and Sensor Runout on Rigid by AMB's*, Proc. of the 5th Int. Symp. on Magnetic Suspension Technology, Santa Barbara, CA, 1999.
5. Setiawan, J. D., Mukherjee, R., Maslen, E. H., and Song, G., *Adaptive Compensation of Sensor Runout and Mass Unbalance in Magnetic Bearing Systems*, Proc. IEEE/ASME Int. Conf. on Adv. Intelligent Mechatronics, Atlanta, GA, 1999.
6. Chen, D., and Paden, B., *Adaptive Linearization of Hybrid Step Motors: Stability analysis*, IEEE Trans. on Automatic Control., Vol.38, No.6, pp.874-887, 1993.
7. Khalil, H., *Nonlinear Systems*, 2nd Ed., Prentice Hall, Upper Saddle River, NJ 07458, 1996.